

LETTER TO THE EDITOR

This Ionization Rate is Just Right: The Impact of Cosmic-Ray Attenuation on the Carbon Cycle Emission in Molecular Clouds

Brandt A. L. Gaches^{1,2*}, Thomas G. Bisbas¹, and Shmuel Bialy³

¹ I. Physikalisches Institut, Universität zu Köln, Zùlpicher StraÙe 77, 50937, Köln, Germany

² Center of Planetary Systems Habitability, The University of Texas at Austin, USA

³ Department of Astronomy, University of Maryland, College Park, MD 20742, USA

Accepted XXX. Received YYY; in original form ZZZ

ABSTRACT

Context. Observations of carbon cycle species, C, C⁺, CO are commonly used to diagnose gas properties in the interstellar medium but are significantly sensitive to the cosmic-ray ionization rate. However, chemical models commonly assume a constant cosmic-ray ionization rate in the clouds.

Aims. We investigate the effect of cosmic-ray attenuation on the emission of carbon cycle species from molecular clouds.

Methods. We use a post-processed chemical model of a simulated dense molecular cloud and quantify the variation in both column densities and velocity integrated line emission of the carbon cycle with different cosmic-ray ionization rate models.

Results. We find that the deviations in the column density for each of the species can be significant and complex. We show that using a constant ionization rate derived from a mass-weighted average of a physically motivated model, $\zeta_c = 2 \times 10^{-16} \text{ s}^{-1}$, can well-reproduce the emission of [C I] $^3P_1 \rightarrow ^3P_0$ at $609 \mu\text{m}$, ^{12}CO ($J = 1 - 0$) emission and the [C II] $158 \mu\text{m}$ emission of the attenuated cosmic-ray ionization rate model.

Conclusions. We conclude by recommending the use of depth-dependent cosmic-ray ionization rate in molecular clouds in multi-line observations, or a tailored constant ionization rates derived from depth-dependent parameterizations.

Key words. Astrochemistry - ISM: abundances - ISM: clouds - (ISM:) cosmic rays - ISM: molecules

1. Introduction

Molecular clouds are flooded by energetic, charged particles, called cosmic rays (CRs), accelerated in shocked environments throughout the galaxy (Grenier et al. 2015; Padovani et al. 2020). In dense molecular gas, well-shielded from ultraviolet radiation, CRs are the dominant source of ionization. In particular, the ionization is dominated by protons with energies between 1 MeV – 1 GeV and secondary electrons produced by primary protons (Dalgarno 2006).

Through the CR ionization of H₂ and formation of H₃⁺, subsequent proton-transfer reactions lead to a diverse zoo of molecular chemistry e.g., HCO⁺, CO, H₂O and NH₃, as well as initiating the deuteration process (see e.g. Tielens 2005; Dalgarno 2006; Bayet et al. 2011; Bialy & Sternberg 2015; Bisbas et al. 2015; Gaches et al. 2019). CR ionization also act as a source of heating in dense gas. Thus, the CR ionization rate (CRIR), denoted ζ (units H₂ ionizations per sec), is one of the most fundamental parameters in astrochemical modeling.

Despite the importance of the CRIR, it is often treated simply with the assumption of a single constant rate. However, low-energy CRs rapidly lose energy as they propagate through molecular gas through Coulomb interactions, ionizations, and pion production (Padovani et al. 2009).

There have been several parameterizations of the attenuation of the CRIR as a function of the hydrogen column

density, hereafter denoted $\zeta(N)$ (e.g. Padovani et al. 2009, 2018; Silsbee & Ivlev 2019). Several astrochemical models have included such prescriptions in one-dimensional astrochemical models (e.g. Rimmer et al. 2012; Owen et al. 2021; Redaelli et al. 2021). While including CR transport (at least high-energy CR transport) has started to become more standard in galactic-scale simulations, to the authors knowledge the inclusion of CR energy losses (and thus a CRIR gradient) has yet to be included in three-dimensional astrochemical models.

In this study, we include a prescription for $\zeta(N)$ in a post-processed three-dimensional astrochemical model of a molecular cloud. In particular, we investigate the impact of the resulting complex three-dimensional CRIR gradients on the abundances and emission from the carbon cycle species, C, C⁺, CO. In §2, we describe the astrochemical CR dominated region (CRDR) model and our prescription for $\zeta(N)$. In §3, we discuss the results of our model analysis. We conclude in §4.

2. Methods

We use the density and velocity distributions of the ‘dense’ cloud model presented in Bisbas et al. (2021), which is a sub-region taken from the Wu et al. (2017) MHD simulations. The simulation domain is a cube of side length, $L = 14 \text{ pc}$, total mass, $M_{\text{tot}} = 4.3 \times 10^4 M_{\odot}$, mean H-nucleus number density $\langle n_{\text{H}} \rangle \equiv M_{\text{tot}}/L^3 \sim 640 \text{ cm}^{-3}$ and

* E-mail: gaches@ph1.uni-koeln.de

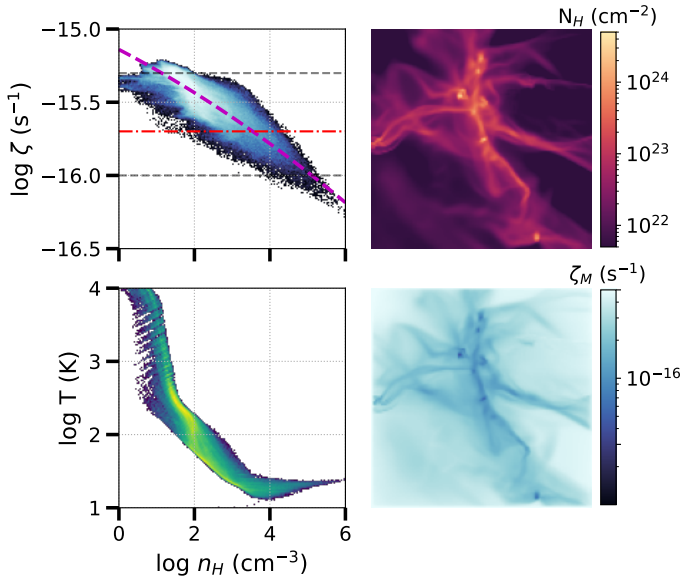


Fig. 1: Top left: The 2D distribution of the CRIR ζ , versus the hydrogen nuclei number density, n_H in our simulation. The red line shows the mass weighted CRIR and the black lines are the two constant ζ models we consider in our comparison. The magenta dashed line shows a fit to the distribution (see Eqn. 4). Bottom left: The temperature-density 2D distribution for the $\zeta(N)$ model. Top right: A 2D map of the hydrogen column density in the simulation. Bottom right: A 2D map of the mass-weighted CRIR, along the line of sight.

mean (observed) column density, $\langle N_{\text{tot}} \rangle \equiv \langle \int n_H(z) dz \rangle \sim 2.91 \times 10^{22} \text{ cm}^{-2}$ resolved with a total number of 112^3 uniform cells.

For this cloud, we compute the atomic and molecular abundances, $x(i) = n(i)/n_H$, for species i , level populations and gas temperature using the publicly available astrochemical code² 3D-PDR (Bisbas et al. 2012). We adopt a subset of the UMIST 2012 chemical network (McElroy et al. 2013), which consists of 33 species and 330 reactions, and standard ISM abundances at solar metallicity ($n_{\text{He}}/n_H = 0.1$, $n_{\text{C}}/n_H = 10^{-4}$, $n_{\text{O}}/n_H = 3 \times 10^{-4}$; Cardelli et al. 1996; Cartledge et al. 2004; Röllig et al. 2007). We use an external isotropic FUV intensity of $G_0 = 10$ (normalized according to Habing 1968), a metallicity of $Z = 1 Z_{\odot}$ and a microturbulent dispersion velocity of $v_{\text{turb}} = 2 \text{ km s}^{-1}$ to be consistent with Bisbas et al. (2021). Furthermore, to construct the emission maps of cooling lines we solve the equation of radiative transfer using the approach presented in Bisbas et al. (2017), with updates presented in Bisbas et al. (2021) to account for dust emission/absorption.

Cosmic-ray attenuation is included using the prescription for the CRIR versus hydrogen column density, $\zeta(N)$, from Padovani et al. (2018), such that

$$\log_{10} \zeta(N) = \sum_{k \geq 0} c_k \log_{10}^k N_{\text{H,eff}}, \quad (1)$$

¹ Hereafter, we refer to species abundances and densities through parentheses, and to elemental abundances through subscripts.

² <https://uclchem.github.io/3dpdr/>

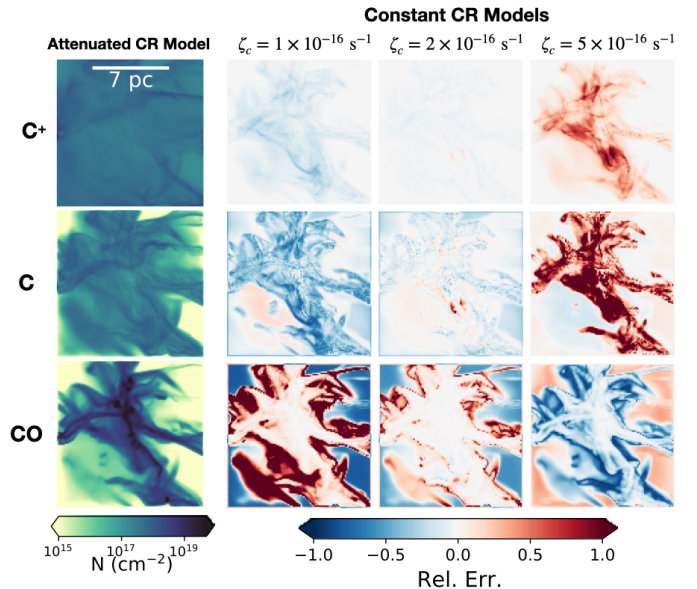


Fig. 2: First column: Column densities of ionized carbon (top), neutral carbon (middle) and carbon monoxide (bottom) for our non-constant $\zeta(N)$ model. Second to Fourth columns: The relative difference (see Eqn. 5) in column density for a constant CRIR with respect to the $\zeta(N)$ model for each of the aforementioned species.

where the coefficients c_k are taken from Table F.1 of Padovani et al. (2018). We use the \mathcal{H} model, which reproduces the AMS-02 high-energy CR spectrum and adjusts the low energy spectrum, below $E < 1 \text{ GeV}$, to reproduce the CRIR inferred in diffuse gas (e.g. Indriolo & McCall 2012; Indriolo et al. 2015; Neufeld & Wolfire 2017). For $N_{\text{H,eff}}$, we utilize the effective (local) hydrogen column density computed as part of the radiation transfer calculations in 3D-PDR,

$$N_{\text{H,eff}} = -\frac{1}{2.5} \ln \left(\frac{1}{\mathcal{N}_r} \sum_{i=1}^{\mathcal{N}_r} e^{-2.5 N_{\text{H},i}} \right), \quad (2)$$

where we sum over the $\mathcal{N}_r = 12$ HEALPix rays of the zeroth level onto which the hydrogen number density is projected and summed along (see Bisbas et al. 2012 for details). While the true column density should take into account the propagation along potentially twisted magnetic field lines, our assumption allows for a first examination of the impact of CR attenuation in three-dimensions and represents a case where the magnetic field lines are not significantly tangled (valid for $n_H \leq 10^9 \text{ cm}^{-3}$, see Padovani et al. 2013). We compare our CR-attenuated CRDR model with four constant-CR models, $\zeta_c = (1, 2, 5, 10) \times 10^{-16} \text{ s}^{-1}$. The particular $\zeta_c = 2 \times 10^{-16} \text{ s}^{-1}$ rate corresponds to the mass-weighted CRIR in the domain, calculated using the $\zeta(N)$ model.

The left panels of Fig. 1 show 2D histograms of $\zeta - n$ and $T - n$ in our simulations, hereafter, “phase diagrams”. The right panels show 2D projections through the simulation, showing the gas column density and the line-of-sight mass-weighted CRIR, ζ_w ,

$$\zeta_M(x, y) = \frac{\int n_H(x, y, z) \zeta(x, y, z) dz}{\int n_H(x, y, z) dz}. \quad (3)$$

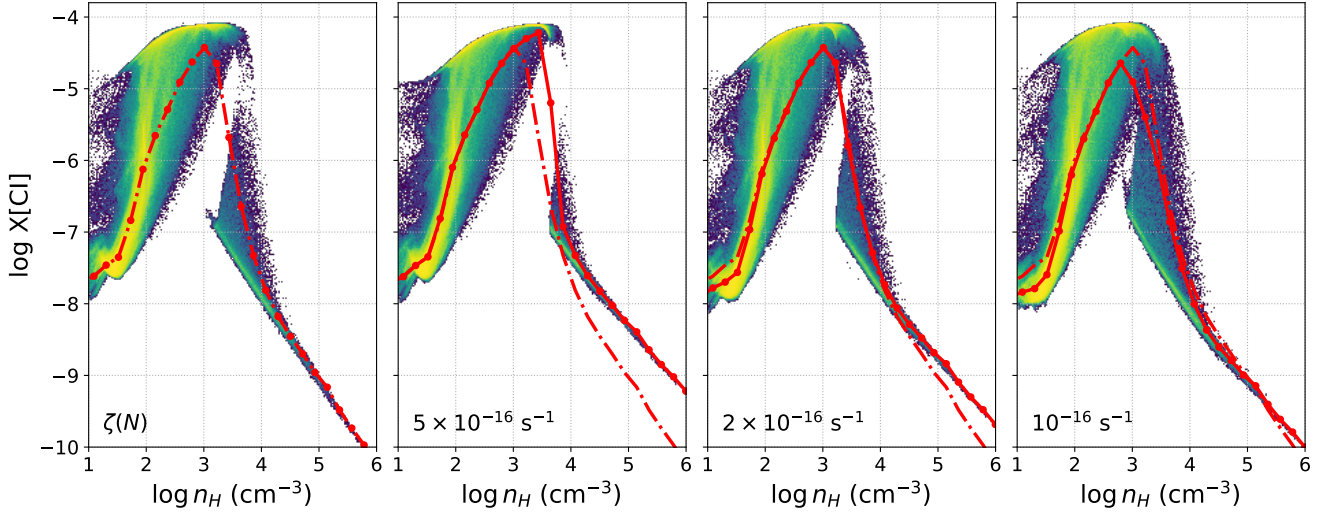


Fig. 3: C abundance, $x(C)$ versus hydrogen nuclei density, n_H . The cosmic-ray model is annotated in each panel. The red lines denote the binned averaged abundance profiles in log-log space. The dashed-dotted lines shows the $\zeta(N)$ abundance profile for comparison.

The CRIR phase diagram (top-left) shows that diffuse regions, with low density, encounter a CRIR an order of magnitude greater than at the highest densities. The overall trends can be explained by a self-gravitating cloud with turbulence induced porosity, such that lower density gas is more likely to be closer to the edge of the domain and dense gas embedded in the cloud. Although $\zeta_c = 5 \times 10^{-16} \text{ s}^{-1}$ may represent the *average* CRIR, it does not represent the CRIR of the majority of the mass of the exhibits. A polynomial fit in log-log space of $\zeta(n_H)$ yields

$$\log \zeta \approx -6.71 \times 10^{-3} \log^2 n_H - 0.134 \log n_H - 15.14. \quad (4)$$

where ζ is in s^{-1} and n_H is in cm^{-3} .

3. Results and Discussion

3.1. Impact on the Distribution of Carbon Cycle Species

We will first discuss the impact of CR attenuation on the distribution of C^+ , C and CO. Figure 2 shows the column densities of C^+ , C and CO for the $\zeta(N)$ model and the relative differences in the column densities, defined by

$$\varepsilon(N_i) = \frac{N_{i,\zeta_c} - N_{i,\zeta(N)}}{N_{i,\zeta(N)}}, \quad (5)$$

for a given species, i , with constant CRIR, ζ_c relative to the $\zeta(N)$ model. We find that the $\zeta_c = 5 \times 10^{-16} \text{ s}^{-1}$ model significantly overproduces C^+ and C and under-produces CO, while the $\zeta_c = 10^{-16} \text{ s}^{-1}$ model under-produces C^+ and C but overproduces CO. The model with $\zeta_c = 2 \times 10^{-16} \text{ s}^{-1}$ has the minimal error. The behavior of CO is interesting; the $\zeta_c = 5 \times 10^{-16} \text{ s}^{-1}$ model over produces CO in diffuse regions while under-producing CO in a thin zone surrounding the dense gas structures. This trend is flipped for the $\zeta_c = 2 \times 10^{-16}$ and $5 \times 10^{-16} \text{ s}^{-1}$ models. At high densities, the CO distributions are effectively identical.

Figure 3 shows 2D histograms of $x(C) - n$ for our various simulations with the bin-averages as red lines. We see a confirmation of the general known behavior of the carbon

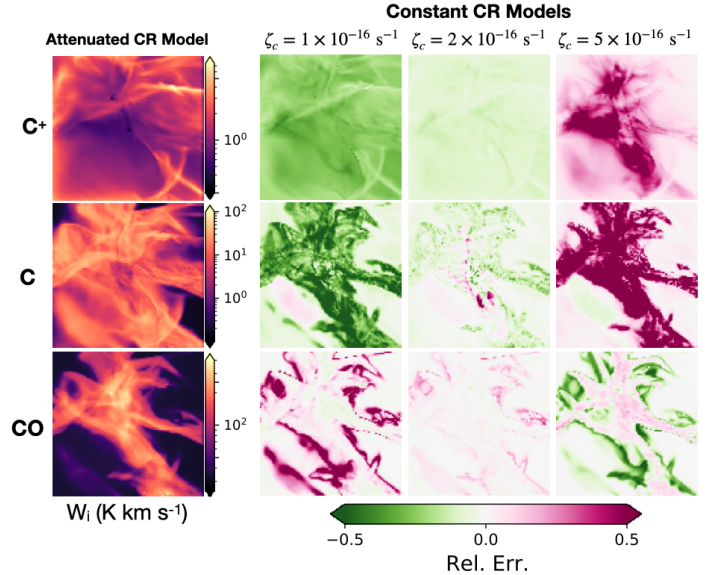


Fig. 4: First column: Velocity integrated emission of the [CII] 158 μm (top), [CI] 609 μm (middle) and CO (1-0) (bottom) emission in units of (K km s^{-1}) . Second to Fourth columns: Relative emission for the different constant cosmic-ray ionization rate models with respect to the $\zeta(N)$ model.

cycle: as the density increases, first C increases (towards $n_H \sim 10^3 \text{ cm}^{-3}$, corresponding to an effective visual extinction of $A_{V,\text{eff}} \sim 2 - 5 \text{ mag}$; Bisbas et al. 2019; Hu et al. 2021) as C^+ efficiently recombine at high densities. Then, as the density continues to increase, C falls as CO formation kicks in.

Comparing the different panels, we see that at low densities there is no difference between the C abundance in the $\zeta(N)$ and $\zeta_c = 5 \times 10^{-16} \text{ s}^{-1}$ models. At number densities between $10^3 < n_H < 10^4 \text{ cm}^{-3}$, the $\zeta(N)$, $\zeta_c = 2 \times 10^{-16}$ and 10^{-16} s^{-1} models exhibit a heightened spread in $x(C)$ compared to $\zeta_c = 5 \times 10^{-16} \text{ s}^{-1}$. Further, at these densi-

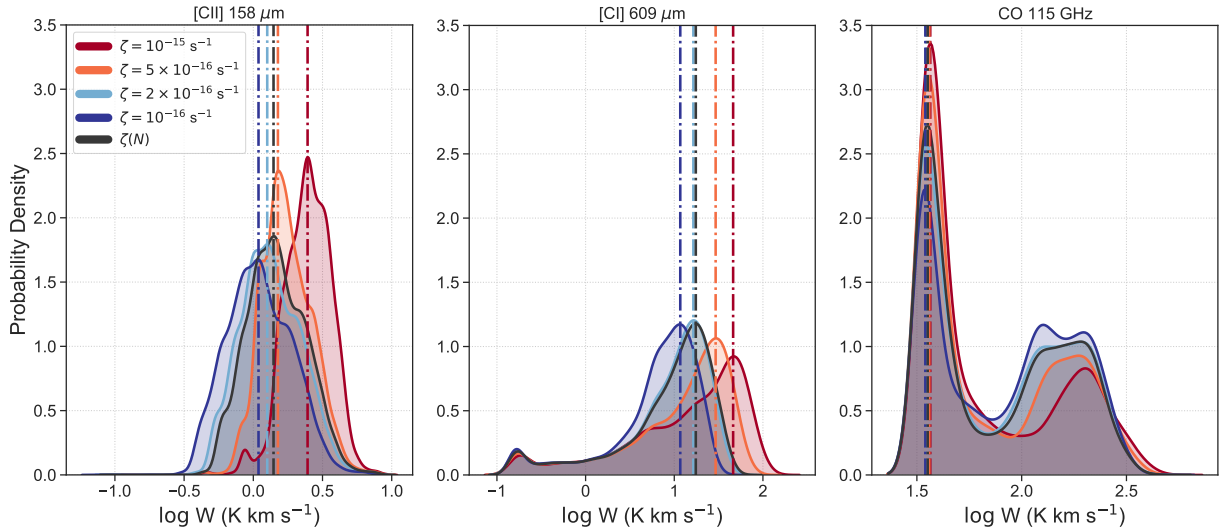


Fig. 5: PDFs of the velocity integrated emission of [CII] 158 μm (right), [CI] 609 μm (center), and CO (1-0) (right) for the different ionization rate models. The vertical lines highlight the peak emission.

ties, the average C abundance profile for $\zeta(N)$ is identical to $\zeta_c = 2 \times 10^{-16} \text{ s}^{-1}$. At high densities, the $\zeta(N)$ average C abundance profile best matches the $\zeta_c = 10^{-16} \text{ s}^{-1}$ model. *Thus, no single constant CRIR matches the average carbon abundance profile across all density regimes, although $\zeta_c = 2 \times 10^{-16} \text{ s}^{-1}$ matches over region encompassing the majority of the mass.* We see that the C-CO transition region is much more spread out for the $\zeta(N)$ and the lower CRIR models. For these CRIR models, the CO dissociation front is not well defined by the density alone.

3.2. Variations in the Observed Emission

We now investigate the impact of CR attenuation on the velocity integrated line emissions of [CII] 158 μm , [CI] $^3P_1 \rightarrow ^3P_0$ at 609 μm and the $^{12}\text{CO } J = 1 - 0$ (hereafter ‘CO (1-0)’) rotational transition at 115.27 GHz. Figure 4 shows the [CI] 609 μm and CO (1-0) integrated emission and the relative errors of these with different constant CRIRs compared to the $\zeta(N)$ model.

We find that the $5 \times 10^{-16} \text{ s}^{-1}$ model is overly bright in [CII] 158 μm and [CI] 609 μm while 10^{-16} s^{-1} is too dim. For [CI] 609 μm there is a low-density pocket in which these trends are flipped. For CO (1-0), the $\zeta_c = 5 \times 10^{-16} \text{ s}^{-1}$ model is too dim in diffuse gas regions, while being over-bright in dense gas (compared to the $\zeta(N)$ model). This trend is flipped in the $\zeta_c = 10^{-16} \text{ s}^{-1}$ model.

Figure 5 shows probability density functions (PDFs) of the distribution of the emission of [CII] 158 μm , [CI] 609 μm and CO (1-0). For [CI] 609 μm , the distribution at the low-end is nearly identical, while there are significant deviations for bright regions. The peak brightness changes drastically with different constant ionization rates, highlighting the issues with modeling C chemistry and emission with a constant ionization rate. However, the distributions of the [CI] 609 μm emission for the $\zeta(N)$ and $\zeta_c = 2 \times 10^{-16}$ models are nearly identical. This trend is matched by the CO emission, where there is a broad distribution of high emission which is very sensitive to the constant CRIR chosen. For the [CII] 158 μm emission, none of the constant CRIR

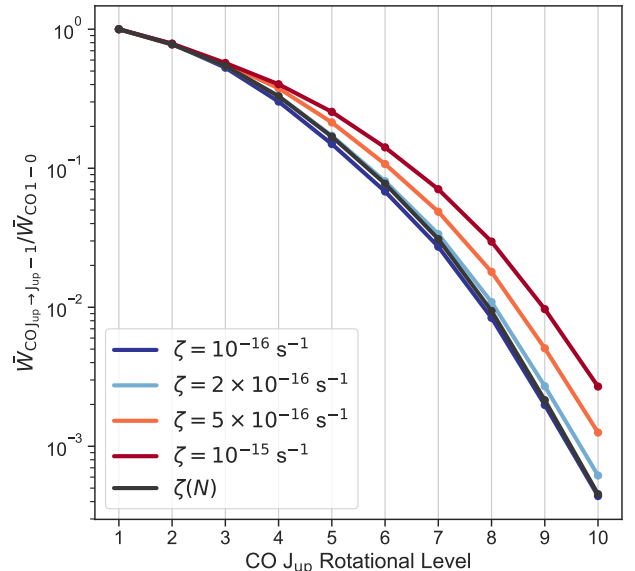


Fig. 6: CO line ratios between higher excitation transitions and the ground transition for the different cosmic-ray ionization rate models.

models well represents the distribution in the $\zeta(N)$ model, although the mass-weighted $\zeta_c = 2 \times 10^{-16} \text{ s}^{-1}$ best matches both the peak and the distribution.

The physical reason behind the changing [CI] 609 μm emission peaks lies in the contrast between the gas temperature and the excitation temperature. The decrease in the emission peak is due to the dense-gas ($n_{\text{H}} > 10^3 \text{ cm}^{-3}$) temperature dropping below $h\nu/k_{\text{B}} \simeq 23.1 \text{ K}$, the excitation temperature of the [CI] forbidden-line emission at 609 μm (see Appendix A). Thus, choosing a CRIR to match the diffuse gas will produce higher temperatures in the dense gas.

Finally, we show in Figure 6 the CO Spectral Line Energy Distribution (SLED) for the different CRIR models.

We find that for low- J transitions, all the ζ_c models well reproduce the line ratios. However, towards higher- J transitions, the differences become more discrepant, due to the attenuation of the CRs resulting in different temperature distributions in dense gas. The $\zeta_c = 10^{-16}$ and $2 \times 10^{-16} \text{ s}^{-1}$ models give the best agreement with the $\zeta(N)$ model, while the higher ζ_c models produce too much high J-CO excitation. This is because these lower CRIR models have a mass-weighted mean temperature that is quite similar to the one seen in the $\zeta(N)$ model (see Appendix).

4. Conclusions

We have presented an analysis of a post-processed photo-dissociation region model of a dense molecular cloud in which we have included a prescription of the CRIR as a function of the local hydrogen column density, $\zeta(N)$. We find the following:

1. The column densities of the carbon cycle species, C^+ , C and CO , are significantly influenced by the inclusion of $\zeta(N)$ versus utilizing a constant ionization rate model. This effect is particularly strong for intermediate density structures, and more negligible at high densities.
2. The CRIR gradient seen through a strong trend with large dispersion as a function of the density produces a wide spread in the abundance of C at intermediate number densities, $10^3 \leq n_H \leq 10^4 \text{ cm}^{-3}$, smoothing out the CO dissociation front in density space.
3. We demonstrate that the overall velocity integrated emission of many species can be potentially changed by imposing a column density dependent CRIR model, not only due to changes in the abundances, but also in the temperatures of the dense gas ($> 10^3 \text{ cm}^{-3}$) as a result of the volumetric nature of cosmic ray heating.

Overall, we highly recommend utilizing physically motivated models of the CRIR in molecular gas, such as polynomial functions of the local number density (Eqn. 4), the column density, $\zeta(N) \propto N^\alpha$ (e.g. Padovani et al. 2009; Silsbee & Ivlev 2019), or more complicated prescriptions (e.g. Padovani et al. 2018; Owen et al. 2021). While utilizing a constant ionization rate ($\zeta_c = 2 \times 10^{-16} \text{ s}^{-1}$) derived from a mass-weighted average produced sensible results for [C] 609 μm and CO (1-0) for Milky Way studies, it may still produce sizable errors in the emission of other lines, such as [CII], due to changes in both the abundances and temperatures.

Acknowledgements. The following PYTHON packages were utilized: NUMPY (Harris et al. 2020), SCIPY (Virtanen et al. 2020), MATPLOTLIB (Hunter 2007), DATASHADER, CMOCEAN. BALG acknowledges support by the ERC starting grant No. 679852 ‘RADFEEDBACK’. TGB acknowledges support from Deutsche Forschungsgemeinschaft (DFG) grant No. 424563772.

References

Bayet, E., Williams, D. A., Hartquist, T. W., & Viti, S. 2011, MNRAS, 414, 1583
 Bialy, S. & Sternberg, A. 2015, MNRAS, 450, 4424
 Bisbas, T. G., Bell, T. A., Viti, S., Yates, J., & Barlow, M. J. 2012, MNRAS, 427, 2100
 Bisbas, T. G., Papadopoulos, P. P., & Viti, S. 2015, ApJ, 803, 37
 Bisbas, T. G., Schrubba, A., & van Dishoeck, E. F. 2019, MNRAS, 485, 3097

Bisbas, T. G., Tan, J. C., & Tanaka, K. E. I. 2021, MNRAS, 502, 2701
 Bisbas, T. G., Tanaka, K. E. I., Tan, J. C., Wu, B., & Nakamura, F. 2017, ApJ, 850, 23
 Cardelli, J. A., Meyer, D. M., Jura, M., & Savage, B. D. 1996, ApJ, 467, 334
 Cartledge, S. I. B., Lauroesch, J. T., Meyer, D. M., & Sofia, U. J. 2004, ApJ, 613, 1037
 Dalgarno, A. 2006, Proceedings of the National Academy of Science, 103, 12269
 Gaches, B. A. L., Offner, S. S. R., & Bisbas, T. G. 2019, ApJ, 878, 105
 Grenier, I. A., Black, J. H., & Strong, A. W. 2015, ARA&A, 53, 199
 Habing, H. J. 1968, Bull. Astron. Inst. Netherlands, 19, 421
 Harris, C. R., Millman, K. J., van der Walt, S. J., et al. 2020, Nature, 585, 357
 Hu, C.-Y., Sternberg, A., & van Dishoeck, E. F. 2021, arXiv e-prints, arXiv:2103.03889
 Hunter, J. D. 2007, Computing in Science & Engineering, 9, 90
 Indriolo, N. & McCall, B. J. 2012, ApJ, 745, 91
 Indriolo, N., Neufeld, D. A., Gerin, M., et al. 2015, ApJ, 800, 40
 McElroy, D., Walsh, C., Markwick, A. J., et al. 2013, A&A, 550, A36
 Neufeld, D. A. & Wolfire, M. G. 2017, ApJ, 845, 163
 Owen, E. R., On, A. Y. L., Lai, S.-P., & Wu, K. 2021, ApJ, 913, 52
 Padovani, M., Galli, D., & Glassgold, A. E. 2009, A&A, 501, 619
 Padovani, M., Hennebelle, P., & Galli, D. 2013, A&A, 560, A114
 Padovani, M., Ivlev, A. V., Galli, D., & Caselli, P. 2018, A&A, 614, A111
 Padovani, M., Ivlev, A. V., Galli, D., et al. 2020, Space Sci. Rev., 216, 29
 Redaelli, E., Sipilä, O., Padovani, M., et al. 2021, arXiv e-prints, arXiv:2109.08169
 Rimmer, P. B., Herbst, E., Morata, O., & Roueff, E. 2012, A&A, 537, A7
 Röllig, M., Abel, N. P., Bell, T., et al. 2007, A&A, 467, 187
 Silsbee, K. & Ivlev, A. V. 2019, ApJ, 879, 14
 Tielens, A. G. G. M. 2005, The Physics and Chemistry of the Interstellar Medium
 van der Tak, F. F. S., Black, J. H., Schöier, F. L., Jansen, D. J., & van Dishoeck, E. F. 2007, A&A, 468, 627
 Virtanen, P., Gommers, R., Oliphant, T. E., et al. 2020, Nature Methods, 17, 261
 Wu, B., Tan, J. C., Nakamura, F., et al. 2017, ApJ, 835, 137

Appendix A: Dense-Gas Temperature Distributions

We investigate the response of the gas temperature in the $n_H \geq 10^3 \text{ cm}^{-3}$ regime with increasing ζ . Figure A.1 shows temperature PDFs for the various simulations including all cells with densities $n_H \geq 10^3 \text{ cm}^{-3}$. As expected, the distributions follow the trend that higher constant ionization rates produce warmer gas. However, none of the constant ionization rate models are able to reproduce the gas temperature distribution of the $\zeta(N)$ model. For observational tracers of the dense gas, the chosen ionization rate may have significant impact on the model emission. Table A.1 shows the mass-weighted gas temperature, $\langle T \rangle_M = (\sum_i T_{\text{gas},i} n_{\text{H},i}) / \sum_i n_{\text{H},i}$ (again, only including cells with $n_H \geq 10^3 \text{ cm}^{-3}$). We find that the $\zeta_c = 10^{-16} \text{ s}^{-1}$ and the $2 \times 10^{-16} \text{ s}^{-1}$ models have $\langle T \rangle_M$ closer to the $\zeta(N)$ model. Indeed, the CO SLED for these two models best matches the one of the $\zeta(N)$'s SLED (see §3.2).

Table A.1: Mass-weighted gas temperatures for different cosmic-ray ionization rate models

CRIR Model	$\langle T \rangle_M$ (K)
$\zeta(N)$	20.38
$\zeta_c = 10^{-16} \text{ s}^{-1}$	20.24
$\zeta_c = 2 \times 10^{-16} \text{ s}^{-1}$	20.79
$\zeta_c = 5 \times 10^{-16} \text{ s}^{-1}$	22.64
$\zeta_c = 10^{-15} \text{ s}^{-1}$	25.40

We highlight the impact of these small changes within the 20-30 K temperature regime that have on higher- J CO transitions for $n_H > 10^3 \text{ cm}^{-3}$. Table A.2 shows radiation temperature (the equivalent blackbody temperature of the emission in the Rayleigh-Jeans limit³) calculations using RADEX (van der Tak et al. 2007) of the CO ladder (up to $J = 10 - 9$) for a gas density of $n_H = 10^4 \text{ cm}^{-3}$ with different gas temperatures, $T = 20$ and 26 K, and with $N(\text{CO}) = 10^{18} \text{ cm}^{-3}$. The aforementioned values are chosen to match with the conditions in the high-density regime as can be seen in Figs.1 and 2. Despite the relatively small difference in the average gas temperature, it has a profound impact on the predictions for the high- J transitions, with deviations up to ~ 40 times for the $J = 10 - 9$ transition. Thus, accurately modeling the temperature of the dense gas is of paramount importance in constraining the physical ISM environment from high- J CO transitions.

Table A.2: RADEX model results for the radiation temperature, T_R (K), of the CO J-ladder for $n_H = 10^4 \text{ cm}^{-3}$.

Temperature (K)	1 – 0	2 – 1	3 – 2	4 – 3	5 – 4	6 – 5	7 – 6	8 – 7	9 – 8	10 – 9
20	16.44	14.70	12.64	10.56	7.91	3.712	0.77	5.59×10^{-2}	2.13×10^{-3}	6.23×10^{-5}
26	22.30	20.47	18.24	15.90	13.07	8.41	3.03	5.55×10^{-1}	4.34×10^{-2}	2.40×10^{-3}

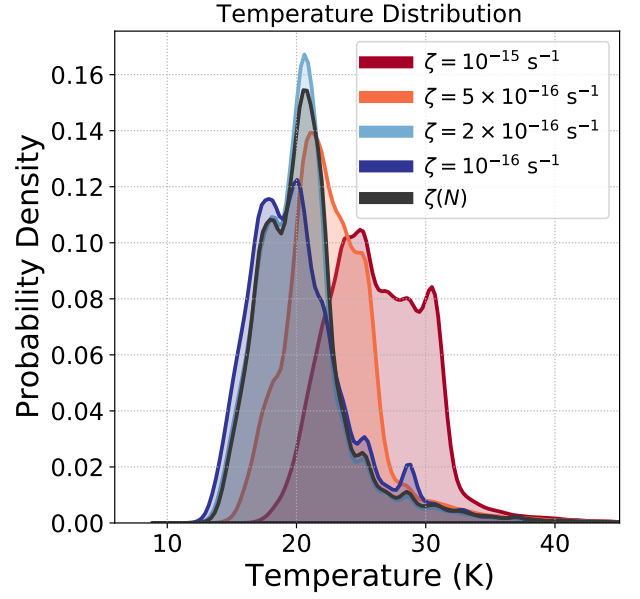


Fig. A.1: Temperature PDFs in the dense gas (all cells with $n_H \geq 10^3 \text{ cm}^{-3}$) for the different CRIR models.

³ RADEX defines this as the main beam antennae temperature with a beam filling factor of unity.